3D closed-loop motion control of swimmer with flexible flagella at low Reynolds numbers

Ali Oulmas[1,2], Nicolas Andreff[2] and Stéphane Régnier[1]

Abstract— **Previously, we developed a 3D path following algorithm to improve the microrobot performances to overcome the modeling errors and environmental disturbances in order to perform real tasks, tested experimentally in a scaled-up helical microswimmer. In this paper, we show that adapting the propulsion mode, the general path following algorithm can be used for any microswimmer behaving as a nonholonomic system. For that purpose, we study a magnetic robot with a flexible tail that mimics the spermatozoa locomotion mechanism. A frequency and amplitude characterization of the flexible swimmer using an oscillating magnetic field is shown. To adapt the propulsion mode, we develop a 3D magnetic field control based on the steering angular velocities which are computed from the path following algorithm in order to propel and steer the flexible robot to reach a desired location in space and achieve for the first time a 3D closed-loop motion control using a swimmer with flexible flagella.**

I. INTRODUCTION

Microswimmers have the potential to optimize certain medical operations and make them mini-invasive such as targeted drug delivery [1] and fertilization assistance [2]. Nowadays, the objects get smaller and become difficult to handle. These microrobots can be used to manipulate, transport and even assemble micro and nanocomponents [3].

At low scale, the locomotion is characterized by low Reynolds numbers because the drag forces from the fluid dominate over the inertia forces. Consequently, the reciprocal motion can not produce net propulsion. Purcel called this the scallop theorem [4]. Microorganisms adapt a nonreciprocal motion in order to propel themselves through the viscous fluid such as the corkscrew-type rotating propulsion and the oscillating propulsion used respectively by E. coli bacteria and spermatozoa. Artificial microrobots mimic the same kind of motion to swim and navigate such as magnetic helical swimmers, which are among the most studied lately. They use a rotating magnetic field and a rigid corkscrew tail [3], [5] or flexible tail [6] in order to advance. In this paper, we are interested in studying a flexible swimmer motion actuated using an oscillating magnetic field. When a magnetic torque is applied on the flexible swimmer, the tail bends and thus produces a thrust force through the interaction with the surrounding viscous fluid.

In the literature, researchers focus on the conception part of microswimmers trying to optimize and adapt the shape to different tasks [2]. However, the control is quite simple and not accurate. A model-based controller is developed in [7] to compensate the artificial swimmer weight. However, since the algorithm is open-loop, it is subjected to errors and drift. In fact, controlling microswimmers in closed-loop will make them less sensitive to environmental disturbances such as thermal noises [8] and boundary effects [9], and will allow to transport microobjects and reach 3D desired locations with more accuracy, robustness and repeatability, which are necessary for performing real tasks. [10] proposes a 2D closed-loop point-to-point motion control of a MagnetoSperm in contact with a solid surface, which consists of generating a uniform magnetic field towards the reference point. However, the swimmer velocity is not continuous at each intermediate point. In the last paper, we proposed a general path following algorithm to improve the performances of these microrobots tested experimentally on a scaled-up helical microswimmer [5]. The controller handles any type of disturbance and allows a smooth convergence of the swimmer to the path.

In this paper, as a first contribution, we show that the 3D path following algorithm developed in [5] can be used for any microswimmer behaving like a nonholonomic system in the condition of adapting the propulsion mode specific to the swimmer. For that purpose, we study the 3D swimming and motion characteristics of a continuous flexible tail swimmer under an oscillating magnetic field. The swimming velocity and agility of the flexible swimmer is characterized in function of the frequency and amplitude of the oscillating magnetic field and to adapt the propulsion mode, we developed a 3D steering magnetic control to reach a desired orientation in space, based on the control inputs of the 3D path following algorithm. As a second contribution, we achieve a closed-loop 3D path following using a swimmer with flexible flagella tested experimentally on different 3D curve shapes. A comparison between the closed-loop and open-loop controls is also shown in terms of accuracy. The experimental results show a smooth convergence of the flexible swimmer to the path and an accuracy less than 1.6% of the robot length.

In the remainder of this paper, section II presents the modeling of the flexible swimmer including the magnetic actuation, the sperm number and kinematic equations in the Serret-Frenet frame, and finally, the control law based

*This work was supported by Région Franche-Comté and the French Agence Nationale de la recherche, through the ANR LEMA and ANR Labex ACTION.

[1]A. Oulmas and S. Régnier are with Sorbonne Universités, UPMC University Paris 06, UMR 7222, ISIR, F-75005 Paris, France ali.oulmas@isir.upmc.fr, stephane.regnier@upmc.fr

[2]A. Oulmas and N. Andreff are with FEMTO-ST Institute, CNRS/ University of Franche-Comté/ ENSMM/ UTBM, 25000 Besançon, France nicolas.andreff@femto-st.fr

Preprint submitted to 2017 IEEE/RSJ International Conference on Intelligent Robots and Systems. Received March 1, 2017.

on the chained-form. Afterwards, section III describes the electromagnetic manipulation system used to propel wirelessly the flexible robot, and the 3D steering magnetic controller. Section IV shows the frequency and amplitude characterization of the magnetic flexible swimmer using an oscillating magnetic field. Section V shows the results of applying the 3D path following using visual feedback.

II. Modeling and control

A. Magnetic torque and force

The flexible robot is actuated using an oscillating magnetic field generated thanks to a 3D Helmholtz coils system. As the magnetic field is uniform, the flexible flagella undergoes a magnetic torque $\mathbf{T}_m$ which is given as follows:

$$\mathbf{T}_m = \mathbf{M} \times \mathbf{B} \tag{1}$$

with $\mathbf{M}$ the magnetic moment and $\mathbf{B}$ the external magnetic field. The magnetic torque tends to align the magnetic moment of the flexible robot with the applied magnetic field [11]. Therefore, with an oscillating magnetic field and a flexible tail, the swimmer can advance by converting the oscillation into linear motion. However, if the magnetic field $\mathbf{B}$ is not completely uniform, a magnetic force $\mathbf{F}_m$ can be generated, which is given as:

$$\mathbf{F}_m = \nabla(\mathbf{M} \cdot \mathbf{B}) \tag{2}$$

where ∇ is the gradient operator [11]. The magnetic field gradient is considered as a disturbance which drifts the flexible swimmer from the desired trajectory. The closed-loop control aims to correct these errors.

B. Sperm number

The sperm number S_p is a dimensionless number measuring the importance of the viscous forces on the elastic forces. It is expressed as in [12] by:

$$S_p = \left(\frac{L^4\, \zeta_\perp\, \omega}{A}\right)^{1/4} \tag{3}$$

with L the total length of the elastic flagella, ω the driving frequency of the oscillating magnetic field, $\zeta_\perp$ the normal viscous drag coefficient and A the flagella coefficient stiffness. For a $S_p \ll 1$, the velocity of the swimmer tends toward zero because the tail is not flexible enough to bend and the scallop theorem is applied. In the other side, for $S_p \gg 1$, the oscillations decrease quickly because the fluid viscosity is high. In nature, the spermatozoa swims at $S_p \sim 7$, however, [13] has showed that the propulsion of a flexible filament immersed in a fluid is optimized at $S_p \sim 1$.

Besides, the stiffness of the flagella can be expressed as $A = EI$ with E the flagella young modulus and I the second moment of area. Because of the fluid frag, the flexible robot bends when trying to align with the applied magnetic torque. The flexural rigidity varies along the elastic tail of the swimmer as follows:

$$E\,I\,\frac{dy}{ds} = \int_0^s \tau_s\, ds \tag{4}$$

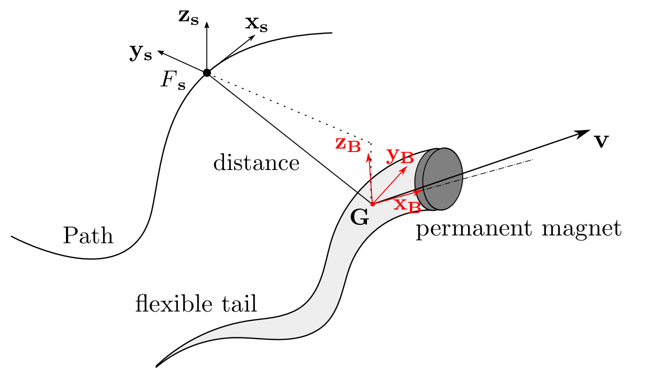

Fig. 1: Flexible swimmer modeling for 3D path following.

where y is the transverse displacement of the tail at s and τ_s is the bending moment.

C. Kinematic equations

The flexible robot is modeled using the body-fixed frame $F_\mathbf{B} = \{\, \mathbf{x_B} \;\; \mathbf{y_B} \;\; \mathbf{z_B} \,\}$ located at the center of mass $\mathbf{G}$, with $\mathbf{x_B}$ the flexible robot principal axis. The swimming plane of the robot is defined by the vectors $\mathbf{x_B}$ and $\mathbf{y_B}$. The flexible robot is driven in 3D space using the direction angle θ_d and the inclination angle θ_i. The former is the average of the robot axis $\mathbf{x_B}$ oscillations in the swimming plane and the latter is the orientation of the swimming plane to the horizontal plane. $\mathbf{x_B}$ is related to θ_d and θ_i as follows:

$$\mathbf{x_B} = [\, S\theta_i \quad C\theta_i\, S\theta_d \quad C\theta_i\, C\theta_d \,] \tag{5}$$

The kinematics of the flexible robot in the Serret-Frenet frame $F_\mathbf{s}$ can be expressed as in [5] by:

$$\begin{aligned}
\dot{s} &= \frac{v\; C\theta_{de}\; C\theta_{ie}}{1 - c\; d_y} && \text{(6a)}\\
\dot{d}_y &= v\; S\theta_{de}\; C\theta_{ie} + \tau\; d_z\; \dot{s} && \text{(6b)}\\
\dot{d}_z &= -\,v\; S\theta_{ie} - \tau\; d_y\; \dot{s} && \text{(6c)}\\
\dot{\theta}_{ie} &= \Omega_y\; C\beta - \Omega_z\; S\beta\; S\alpha - \dot{\alpha}\; C\beta + \tau\; \dot{s}\; S\theta_{de} && \text{(6d)}\\
\dot{\theta}_{de} &= \Omega_z\; \frac{C\alpha}{C\theta_{ie}} + \frac{\dot{\beta}}{C\theta_{ie}} - \tau\; \dot{s}\; T\theta_{ie}\; C\theta_{de} - c\; \dot{s} && \text{(6e)}
\end{aligned}$$

where s, c and τ are respectively the curvilinear abscissa, the curvature and the torsion, θ_{de} and θ_{ie} are respectively the direction and inclination orientation errors between the total linear velocity $\mathbf{v}$ and the tangential vector of $F_\mathbf{s}$, d_y and d_z are the horizontal and vertical distances of $\mathbf{G}$ to the path while Ω_y and Ω_z are the steering angular velocities. α and β are used to compensate lateral disturbances and the flexible swimmer weight. For more details, see [14].

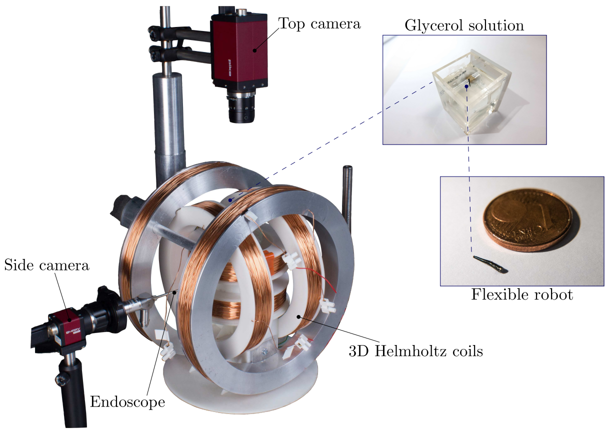

Fig. 2: The magnetic manipulation system used to propel and steer wirelessly the swimmer with flexible flagella.

D. Control law

To design the controller, we introduced in [14] a new chained form to linearize the model in (6) as follows:

$$\dot{x}_1 = u_1 \quad (7a)$$
$$\dot{x}_2 = x_3\, u_1 \quad (7b)$$
$$\dot{x}_3 = u_2 \quad (7c)$$
$$\dot{x}_4 = x_5\, u_1 \quad (7d)$$
$$\dot{x}_5 = u_3 \quad (7e)$$

The variables and inputs transformation is defined as follows:

$$\begin{aligned}(x_1,x_2,x_3,x_4,x_5) &= \big(s,\ d_y,\ (1-c\,d_y)T\theta_{de}+\tau\,d_z,\\ &\quad d_z,\ (c\,d_y-1)T\theta_{ie}C\theta_{de}^{-1}-\tau\,d_y\big)\\ (u_1,u_2,u_3) &= (\dot{s},\ \gamma_{21}\ \Omega_z+\gamma_{22},\\ &\quad \gamma_{31}\ \Omega_y+\gamma_{32}\ \Omega_z+\gamma_{33})\end{aligned} \quad (8)$$

where $\gamma_{..}$ are scalars given in Appendix.

To follow the 3D desired path, the distance and orientation errors are servoed to zero using the following state feedback control law:

$$u_2 = -k_{d1}\,u_1\,x_2 - k_{t1}\,|u_1|\,x_3 \quad (9)$$
$$u_3 = -k_{d2}\,u_1\,x_4 - k_{t2}\,|u_1|\,x_5 \quad (10)$$

where $k_{..}$ are the control gains tuned empirically.

E. Magnetic actuation

III. The Magnetic Manipulation System

The flexible robot consists of a magnetic disc head and an elastic tail (Fig. 2). The latter was made using elastomer obtained after mixing base and catalyst liquids. The length of the flexible tail is about 8mm. The permanent magnet is a 0.8mm diameter and 0.2mm height disc magnet. The magnetization is along the the flexible robot principal axis. During the experiments, the flexible flagella is emerged in a pure glycerol with a density of 1.26g/cm^3 and a viscosity of 1.524Pa.s at 23°C. The swimming velocity of the robot is measured about 1.6mm/s. The Reynolds number is computed about $Re \approx 0.01$.

To propel the flexible robot, a driving oscillating magnetic field $\mathbf{B}_d$ is generated thanks to the 3D Helmholtz system in Fig. 2, and is expressed as explained in [15] by:

$$\mathbf{B}_d = B_x\,\mathbf{x_B} + B_y\,cos(2\pi f t)\,\mathbf{y_B} \quad (11)$$

The swimming plane of the flexible robot is defined by the vectors $\mathbf{x_B}$ and $\mathbf{y_B}$. As the linear motion direction of flexible swimmers does not change with the oscillating magnetic field direction, the homogeneous static magnetic field $\mathbf{B}_x = B_x\,\mathbf{x_B}$ is introduced to control the direction of the flexible robot. A sinusoidal magnetic field $\mathbf{B}_y = B_y\,cos(2\pi f t)\,\mathbf{y_B}$ is applied in the direction perpendicular to the flexible swimmer axis, with f the oscillation frequency. The resulting magnetic field $\mathbf{B}_d$ oscillates around the swimmer axis. As the magnetization $\mathbf{M}$ is in the swimming plane, the driving magnetic torque $\mathbf{T}_d$ is perpendicular to both $\mathbf{M}$ and $\mathbf{B}_d$ and so to the swimming axis.

To reach a desired orientation in space, the steering magnetic field $\mathbf{B}_s$ is developed as follows:

$$\mathbf{B}_s = \frac{\lambda}{\|\mathbf{M}\|}\mathbf{x_B}^* \quad (12)$$

with λ the control gain and $\mathbf{x_B}^*$ the swimmer desired orientation which is related to the real-time orientation $\mathbf{x_B}$ and the steering angular velocity $\mathbf{\Omega}$ as follows:

$$\mathbf{x_B}^* = \mathbf{\Omega}\times\mathbf{x_B}\ dt \quad (13)$$

where dt is the sample time. $\mathbf{\Omega} = (0,\Omega_y,\Omega_z)^T$ is computed using the general path following algorithm by inverting the control inputs u_2 and u_3 in (8) as follows:

$$\begin{aligned}\Omega_z &= (u_2-\gamma_{22})\ \gamma_{21}^{-1}\\ \Omega_y &= \big(u_3-\gamma_{33}-\gamma_{32}\,\gamma_{21}^{-1}\,(u_2-\gamma_{22})\big)\ \gamma_{31}^{-1}\end{aligned} \quad (14)$$

From (1), the steering magnetic torque $\mathbf{T}_s$ is computed as follows:

$$\mathbf{T}_s = \mathbf{M}\times\mathbf{B}_s \quad (15)$$
$$= \|\mathbf{M}\|\,\mathbf{x_B}\times\frac{\lambda}{\|\mathbf{M}\|}\mathbf{x_B}^* \quad (16)$$
$$= \lambda\,\mathbf{x_B}\times\mathbf{x_B}^* \quad (17)$$

to reach the desired orientation, the steering magnetic torque is applied along $\mathbf{x_B}\times\mathbf{x_B}^*$.

To summarize, in order to adapt the propulsion mode specific to the swimmer, the steering magnetic controller should be developed in function of the steering angular velocities and the latter are computed using the general path following control inputs.

IV. Characterization of the Flexible Robot

The goal of this paper is path following using a magnetic flexible swimmer. The frequency and amplitude responses can be used to control the swimming velocity and agility of the robot during the motion control.

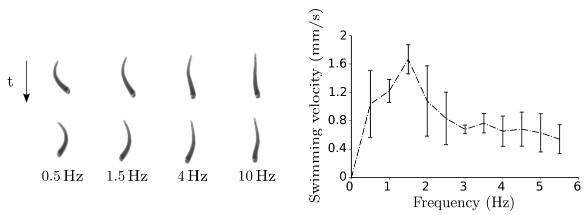

(a) Shape of the swimmer (b) Swimming velocity

Fig. 3: For different oscillation frequencies, the tail shape of the flexible swimmer (a) and the mean of the swimming velocity in the horizontal plane with an inclination angle of $50°$ in order to compensate the weight of the swimmer. The error bars depict the standard deviation.

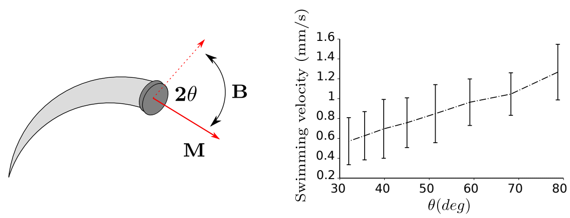

(a) Oscillation amplitude (b) Swimming velocity

Fig. 4: (a) The oscillation amplitude is proportional to the angle 2θ and (b) the oscillation amplitude response of the flexible swimmer. This characterization is realized under an inclination angle of $50°$ and an oscillation frequency of 1.2Hz.

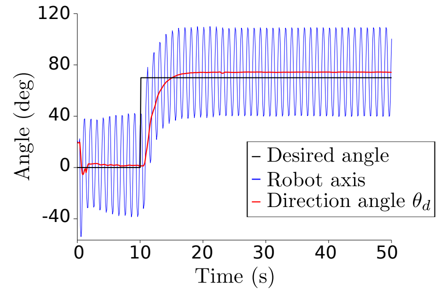

Fig. 5: The flexible robot response to a step angle of $70°$. The direction angle θ_d is computed thanks to the mean of the flexible robot axis oscillations.

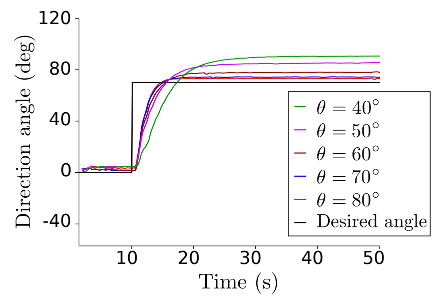

Fig. 6: Step response to the $70°$ direction angle with different magnetic field oscillation amplitudes. The inclination angle and the oscillation frequency are kept fixed during experiments.

1) Frequency analysis: Following the oscillating magnetic field, the flexible tail of the swimmer can bend because of the fluidic drag and thus generate a thrust force in 3D space. Fig. 3 describes the shape and swimming velocity of the flexible robot in a pure glycerol for different frequencies of the oscillating magnetic field. To compensate the weight of the robot, the inclination angle is kept at $50°$ during experiments.

The swimming velocity of the flexible swimmer increases with the oscillating frequency of the magnetic field until the cut-off frequency around 1.5Hz. Beyond this frequency, the swimming velocity decreases slowly as presented in Fig. 3(b). The results are similar to those in [16]. We observed that at high frequencies the flexible tail can not follow the oscillating magnetic field deforming in a nonlinear way as shown in Fig. 3(a).

2) Amplitude analysis: The magnetic flexible swimmer is propelled using an oscillating magnetic torque which tends to align the magnetic moment $\mathbf{M}$ of the robot with the applied magnetic field $\mathbf{B}$. The amplitude of the oscillation is proportional to the angle 2θ where $\theta = atan(B_y/B_x)$ as presented in Fig. 4(a).

It can be seen in Fig. 4(b) that the average of the swimming velocity of the flexible swimmer increases as we increase the magnetic field oscillation amplitude. Below, we show also that the the oscillation amplitude plays a role in the agility of the flexible swimmer.

For that purpose, experiments have been performed using the step response of the flexible robot to a $70°$ direction angle with different oscillation amplitudes as shown in Fig. 6. The direction angle of the robot is calculated using the angle mean of the robot principal axis oscillations as depicted in Fig. 5.

In Fig. 6, it can be seen that the time response of the flexible robot, which is defined as the the time that the swimmer takes to establish a steady state regime, depends strongly on the oscillation amplitude. The response is faster for large oscillations, in addition, the static error at the end of graphs is smaller.

V. Motion control

Once the flexible swimmer is characterized and the propulsion mode is adapted, the general path following algorithm is tested on the prototype with different 3D curve shapes following the procedure in Algorithm 1. The flexible swimmer is oscillating in synchronization with the magnetic field at a frequency of $1Hz$.

Fig. 7 and Fig. 8 depict the 3D reconstruction of the flexible swimmer trajectory while following respectively an inclined sinusoidal and an arbitrary trajectories. It can be seen that the flexible swimmer follows well the trajectory despite the complexity of the paths. The multimedia attach-

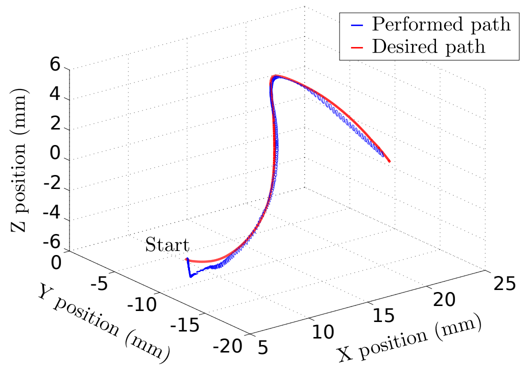

Fig. 7: 3D path following of an arbitrary trajectory shape using the flexible swimmer. The control gains were $k_{d1} = 0.5$, $k_{t1} = 0.2$, $k_{d2} = 0.4$ and $k_{t2} = 0.1$.

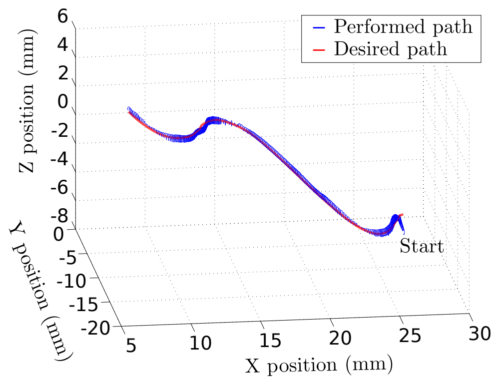

Fig. 8: 3D path following of an inclined sinusoidal trajectory using the flexible swimmer.

ment shows the top and side views of the flexible swimmer following the desired trajectories.

The general path following algorithm consists of minimizing the distance and orientation errors between the flexible swimmer and the reference path. When the flexible swimmer is far from the path, it converges first to the path then goes along the path by following the path tangential vector.

The flexible robot 3D motion was also controlled in open-loop using the same inclined sinusoidal trajectory before. The flexible robot follows the tangential vector of the desired path. The result is drawn in Fig. 9. At the same graph, we depict the trajectory of the flexible robot using the closed-loop control. The oscillation frequency and the weight compensating angle are kept fix during the experiments. It can be seen that the flexible robot follows the trajectory with more accuracy in the case of the closed-loop control by correcting the drift errors caused mainly by the friction between the flexible swimmer and the substrate, the system imperfection and the computing errors of the weight compensating angle. The distance RMS errors during the closed-loop control are $99\mu m$ for d_y and $226\mu m$ for d_z. These experiments show the robustness and accuracy of the closed-loop control which can be used to perform real tasks at low scale by compensating

Algorithm 1: 3D closed-loop control of the flexible swimmer

Require: $f_{min} \leq f \leq f_{max}$
$v \leftarrow total\_linear\_speed$
$\mathcal{C}(s) \leftarrow$ 3D_geometric_path
while not end of the path **do**
$I,\ I_1 \leftarrow$ grab_images()
$\mathbf{G},\ \mathbf{x_B} \leftarrow$ swimmer_tracking($I,\ I_1$)
$\mathbf{S} \leftarrow$ projection_path($\mathbf{G}$)
$(\mathbf{x_F}, \mathbf{y_F}, \mathbf{z_F}) \leftarrow$ Serret_Frenet_frame
$(s,\ c,\ \tau,\ \frac{d\ c}{ds},\ \frac{d\ \tau}{ds}) \leftarrow$ path_parameters
$(d_z,\ d_y) \leftarrow$ distance_errors
$(\theta_{de},\ \theta_{ie}) \leftarrow$ orientation_errors
$(\dot{s},\ \dot{d}_y\ \dot{d}_z,\ \dot{\theta}_{de},\ \dot{\theta}_{ie}) \leftarrow$ kinematic_equations, (6)
$(\gamma_{21},\ \gamma_{22},\ \gamma_{31},\ \gamma_{32},\ \gamma_{33}) \leftarrow$ scalars
$(u_1,\ u_2,\ u_3) \leftarrow$ control_law, (8), (9) and (10)
$(\Omega_y,\ \Omega_z) \leftarrow$ angular_velocities, (14)
$\mathbf{B}_d \leftarrow$ driving_magnetic_field($\mathbf{x_B},\ \mathbf{y_B}$), (11)
$\mathbf{B}_s \leftarrow$ steering_magnetic_field($\mathbf{x_B},\ \boldsymbol{\Omega}$), (12)
$(U_S,\ U_M,\ U_B) \leftarrow$ tension_conversion($\mathbf{B}_d,\ \mathbf{B}_s$)
end while

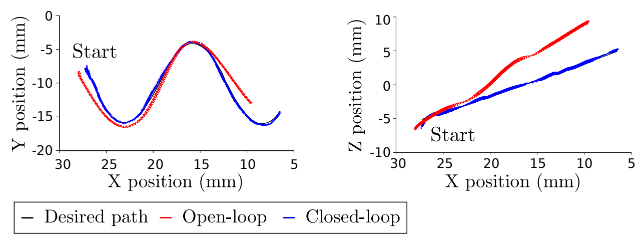

(a) Top view (b) Side view

Fig. 9: Comparison between the open-loop and closed-loop controls while following an inclined sinusoidal trajectory using the flexible robot.

the modeling errors and the environmental disturbances such as boundary effects.

The general path following algorithm was tested previously on a helical swimmer actuated with a rotating magnetic field [5]. In this paper, we adapted the magnetic controller for the flexible swimmer by following an oscillating magnetic field rather than a rotating magnetic field. The results show that the controller is still efficient, robust and accurate. In this section, we demonstrated that the controller can be used for any microswimmer behaving as a nonholonomic system, which means that the microswimmer should advance in the direction of its principal axis with the lateral displacements nulls exactly as a mobile robot in 2D or an autonomous underwater vehicle in space.

VI. CONCLUSIONS

In this paper, we achieve a 3D closed-loop motion control using a swimmer with flexible flagella for the first time according to our best knowledge. First, the swimmer with flexible tail is characterized in function of the frequency and amplitude of the oscillating magnetic field. Furthermore, we developed a 3D steering magnetic field control based on the steering angular velocities, which are computed from the general path following that we developed above and we demonstrated that the algorithm can be used for any swimmer behaving as a nonholonomic system in the condition of adapting the propulsion mode specific to the swimmer. Finally, the visual servo control was validated by following trajectories in space. Controlling the flexible robot in closed-loop aims to improve their performances in order to achieve real tasks and make them less sensitive to environmental disturbances which are more important at low scale.

In the future, we intend to control a group of magnetic flexible swimmers to improve their performances such as transporting drugs for diseased cells inside human body and also compare experimentally their performances in terms of stability, rapidity and accuracy with helical swimmers that are actuated with a rotating magnetic field.

APPENDIX

The scalars used to compute the steering angular velocities Ω_y and Ω_z in (14) are given as follows:

$$
\begin{aligned}
\gamma_{21} &= \; v\,\dot{s}^{-1}\,C\theta_{de}^{-1}\,C\alpha \\
\gamma_{22} &= \; v\dot{s}^{-1}C\theta_{de}^{-1}\dot{\beta} - \dot{s}\,\big(2\,v\,\dot{s}^{-1}\,\tau\,S\theta_{ie} + \tau^2 d_y - d_z\tfrac{\partial\tau}{\partial s} \\
&\quad + c(c\,d_y - 1)\,(1 - 2C\theta_{de}^{-2}) + (c\,\tau\,d_z + d_y\tfrac{\partial c}{\partial s})T\theta_{de}\big) \\
\gamma_{31} &= \; -v\,\dot{s}^{-1}\,C\beta\,C\theta_{ie}^{-1} \\
\gamma_{32} &= \; v\,\dot{s}^{-1}\,C\theta_{ie}^{-1}\,(S\alpha\,S\beta - C\alpha\,S\theta_{ie}\,T\theta_{de}) \\
\gamma_{33} &= (1 - cd_y)(\dot{\alpha}C\beta - \dot{\beta}S\theta_{ie}T\theta_{de}) + \dot{s}\Big(d_y\tfrac{\partial c}{\partial s}T\theta_{ie}C\theta_{de}^{-1} \\
&\quad - d_y\tfrac{\partial\tau}{\partial s} - \big(d_z\tau + 2(1 - cd_y)T\theta_{de}\big)\big(\tau + cT\theta_{ie}C\theta_{de}^{-1}\big)\Big)
\end{aligned}
$$

It can be noticed that some scalars depend on the total linear velocity $\mathbf{v}$ and the variation of the sideslip and attack angle respectively $\dot{\beta}$ and $\dot{\alpha}$.

REFERENCES

[1] F. Qiu, S. Fujita, R. Mhanna, L. Zhang, B. Simona and B. Nelson. *Magnetic helical microswimmers functionalized with lipoplexes for Targeted Gene Delivery*. Advanced Functional Materials, vol. 25, no. 11, pp. 1666-1671, 2015.

[2] M. Medina-Sánchez, L. Schwarz, A. Meyer, F. Hebenstreit and O. Schmidt. *Cellular cargo delivery: Towards assisted fertilization by spermCarrying micromotors*. Nano letters, vol. 16, no. 1, pp. 555-561, 2015.

[3] S. Tottori, L. Zhang, F. Qiu, K. Krawczyk, A. Franco-Obregn and B. Nelson. *Magnetic helical micromachines: Fabrication, controlled swimming, and cargo transport*. Advanced Materials, vol. 24, no. 6, pp. 811-816, 2012.

[4] E. Purcell. *Life at low reynolds number*. American Journal of Physics, vol. 45, no. 1, pp. 3-11, 1977.

[5] A. Oulmas, N. Andreff and S. Régnier. *Closed-loop 3D path following of scaled-up helical microswimmers*. IEEE International Conference on Robotics and Automation, pp. 1725-1730, Stockholm, Sweden, 2016.

[6] T. Xu, C. Vong, B. Wang, L. Liu, X. Wu and L. Zhang. *Rotating soft-tail millimeter-scaled swimmers with superhydrophilic or superhydrophobic surfaces*. IEEE International Conference on Biomedical Robotics and Biomechatronics, pp. 502-507, Singapore, 2016.

[7] A. Mahoney, J. Sarrazin, E. Bamberg and J. Abbott. *Velocity Control with Gravity Compensation for Magnetic Helical Microswimmers*. Advanced Robotics, vol. 25, no. 8, pp. 1007-1028, 2011.

[8] A. Ghosh, D. Paria, G. Rangarajan and A. Ghosh. *Velocity fluctuations in helical propulsion: How small can a Propeller Be*. Journal of Physical Chemistry Letters, vol. 5, no. 1, pp. 62-68, 2014.

[9] K. Peyer, L. Zhang, B. Kratochvil and B. Nelson. *Non-ideal swimming of artificial bacterial flagella near a surface*. IEEE International Conference on Robotics and Automation, pp. 96-101, Anchorage, Alaska, USA, 2010.

[10] I. Khalil, K. Youakim, A. Snchez and S. Misra. *Magnetic-based motion control of sperm-shaped microrobots using weak oscillating magnetic fields*. IEEE/RSJ International Conference on Intelligent Robots and Systems, pp. 4686-4691, Chicago, Illinois, USA, 2014.

[11] J. Coey. *Magnetism and magnetic materials*. Cambridge University Press, 2010.

[12] A. Evans and E. Lauga. *Propulsion by passive filaments and active flagella near boundaries*. Physical review, vol. 82, no 4, pp. 041915-1 to 041915-12, 2010.

[13] C. Lowe. *Dynamics of filaments: modelling the dynamics of driven microfilaments*, Philosophical Transactions of the Royal Society of London B: Biological Sciences, vol. 358, no. 1437, pp. 1543-1550, 2003.

[14] A. Oulmas, N. Andreff and S. Régnier. *Chained formulation of 3D path following for nonholonomic autonomous robots in a Serret-Frenet frame*. American Control Conference, pp. 7275-7280, Boston, MA, USA, 2016.

[15] R. Dreyfus, J. Baudry, M. Roper, M. Fermigier, H. Stone and J. Bibette. *Microscopic artificial swimmers*. Nature, vol. 437, no 7060, pp. 862-865, 2005.

[16] J. Espinosa-Garcia, E. Lauga and R. Zenit. *Fluid elasticity increases the locomotion of flexible swimmers*. Physics of Fluids, vol. 25, no. 3, pp. 031701, 2013.